ChemComm

COMMUNICATION

View Article Online
View Journal | View Issue

Cite this: *Chem. Commun.*, 2024, **60**, 7757

Received 17th April 2024,
Accepted 5th June 2024

DOI: 10.1039/d4cc01822b

rsc.li/chemcomm

Synthesis and soft crystal structure-induced broad emission of $(NH_3C_6H_{12}NH_3)InBr_5{\cdot}2H_2O$†

Shuva Biswas,‡[a] Arnab Mandal,‡[a] Diptikanta Swain [b] and Kanishka Biswas *[a]

We report a simple synthesis of a new lead-free zero-dimensional (0D) hybrid halide compound, (5P1)$InBr_5{\cdot}2H_2O$ [(5P1) = $NH_3C_6H_{12}NH_3$], which hosts isolated and distorted octahedra of $[InBr_5(H_2O)]^{2-}$, surrounded by bulky asymmetric organic cations [$(5P1)^{2+}$] and H_2O molecules. The hybrid crystals exhibit broad self trapped excitonic (STE) emission due to strong anharmonic soft structure.

Three-dimensional (3D) lead (Pb) halide perovskites have achieved remarkable advances in solar cells and other optoelectronic applications in recent years.[1–3] However, the stability issues of 3D perovskite halides and toxicity due to presence of Pb have limited their practical applications.[4] Therefore, low-dimensional Pb-free organic–inorganic hybrid halides have become a propitious alternative as a relatively stable luminescent material.[5,6] Reducing dimensionality by disconnecting metal halide octahedra progressively softens the crystal lattice.[7] For instance, zero-dimensional (0D) organic–inorganic hybrid halides possess localized polyhedra, making the lattice remarkably soft.[8] Significant anharmonicity of a soft lattice, coupled with strong electron–phonon coupling, often leads to the formation of self-trapped excitonic (STE) state through transient local lattice distortion upon photoexcitation.[9–11] Furthermore, in 0D metal halides, emission from the STE state is solely dependent on the inorganic luminescent building block.[10,12]

0D hybrid halides are generally classified based on the s^2, d^5 and d^{10} electronic configurations of their central metal cation.[6] The stereochemical expression of the ns^2 lone pair in the central cation (Pb^{2+}, Sn^{2+}, Bi^{3+}, Sb^{3+} *etc.*) prompts the polyhedral distortion to occur within the structure.[13] For example, a recent report on a Bi/Sb-based halide, namely $(C_8NH_{12})_4Bi_{0.57}Sb_{0.43}Br_7{\cdot}H_2O$ with distorted polyhedra, showcases a broadband STE emission ranging from 400 to 850 nm.[14] Conversely, d^5 metal cation (*e.g.* Mn^{2+}) based 0D hybrid halides are known for their typical narrow band emission.[15] However, $(C_4H_9NH_3)_2MnI_4$ shows dual-emissive PL having emission peaks with different intensities.[16] 0D hybrid halides with d^{10} metal systems (Ag^+ and Cu^+) are also a fascinating class of luminescent hybrid halides due to their multiple excited states and diverse structural topologies.[17,18] More recently, there have been reports of stable indium (In)-based 0D halides, such as all-inorganic $Cs_2InBr_5{\cdot}H_2O$,[19] hybrid $(C_4H_{14}N_2)_2In_2Br_{10}$.[20] and $(PMA)_3InBr_6$,[21] that demonstrate promising luminescence properties. Moreover, recent report shows Sb^{3+} doping into all-inorganic $Cs_2InBr_5{\cdot}H_2O$ leads to further increament of bright emissions.[22,23]

Herein, we have synthesized a new 0D organic–inorganic hybrid halide, (5P1)$InBr_5{\cdot}2H_2O$ (5P1 = 1,5-diammonium-2-methylpentane), utilizing a simple acid precipitation technique. This halide showcases a temperature-dependent structural phase transition and broad STE emission. Strong electron–phonon coupling within the lattice, as validated from temperature-dependent PL studies, explains the underlying mechanism of the broad and intense STE emission. Furthermore, Raman spectroscopy and low-temperature heat capacity (C_p) measurement unveil the existence of low-energy optical phonon modes, suggesting the presence of a soft lattice. Sound velocity measurement implies low values of elastic moduli, indicating extreme softness of the 0D hybrid halide lattice and strong anharmonicity. Strong electron–phonon coupling originating from the soft lattice and anharmonicity trigger broad STE emission from (5P1)$InBr_5{\cdot}2H_2O$.

(5P1)$InBr_5{\cdot}2H_2O$ was synthesized using the acid precipitation method by dissolving precursors (metal salt and organic ligand) in HCl with heat treatment to obtain a clear saturated solution. The resulting solution was allowed to cool down slowly for the formation of colourless single crystals (Methods section, ESI†). The hybrid halide compound crystallizes in an orthorhombic system (space group *Pnma*) at room temperature with lattice parameters a = 20.264(3) Å, b = 7.9353(11) Å, c = 11.0226(13) Å and $\alpha = \beta = \gamma = 90^\circ$

[a] *New Chemistry Unit, International Centre for Materials Science and School of Advanced Materials, Jawaharlal Nehru Centre for Advanced Scientific Research (JNCASR), Jakkur P. O., Bangalore 560064, India. E-mail: kanishka@jncasr.ac.in*
[b] *Institute of Chemical Technology-IndianOil Odisha Campus, Bhubaneswar 751013, India*

† Electronic supplementary information (ESI) available. CCDC2348109 and 2348112. For ESI and crystallographic data in CIF or other electronic format see DOI: https://doi.org/10.1039/d4cc01822b

‡ S. B. and A. M. contributed equally.

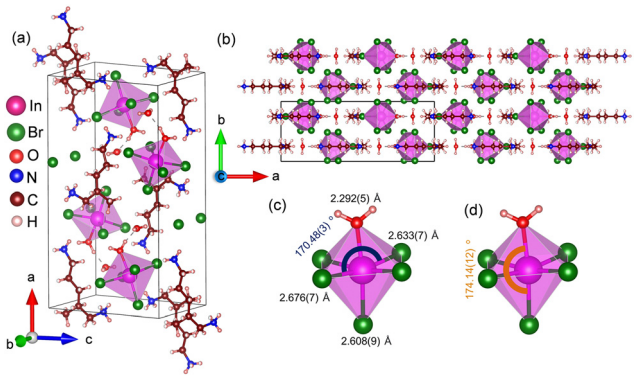

Fig. 1 (a) Crystal structure of (5P1)$InBr_5{\cdot}2H_2O$ viewed down the crystallographic *b*-axis. (b) Extended crystal structure of (5P1)$InBr_5{\cdot}2H_2O$ along the *c*-axis, showcasing its 0D nature. (c) and (d) Coordination environment of indium in an individual octahedron displaying bond length and bond angle values.

(Table S1, ESI† and Fig. 1), as determined using single-crystal X-ray diffraction (SCXRD). As illustrated in Fig. 1a and b, (5P1)$InBr_5{\cdot}2H_2O$ consists of isolated $[InBr_5(H_2O)]^{2-}$ inorganic octahedral units, which are well separated from each other by large $(5P1)^{2+}$ organic cations and lattice H_2O molecules, forming a typical 0D hybrid halide structure. The long distance of 7.85(8) Å between two nearest octahedral units eliminates the possibility of any electronic interaction between them. Each lattice H_2O interacts with the coordinated H_2O of an $[InBr_5(H_2O)]^{2-}$ octahedron through hydrogen bonding (H-bonding) interactions having O–H···O distance of around 1.72 Å. N–H···Br hydrogen bond lengths (2.73 to 2.84 Å) also indicate an interaction between organic and inorganic sublattices (Fig. S1a and Table S2, ESI†). Isolated octahedra are distorted due to indium (In) atoms each being off-centered, arising from shorter In–O bond lengths [2.292(5) Å] compared to that of In–Br bonds [2.608(9)–2.676(7) Å] (Fig. 1c and d). Owing to the distortion, equatorial ∠Br–In–Br [170.48(3)°] and axial ∠Br–In–O [174.14(12)°] deviate from the ideal value of 180° (Fig. 1c and d).

Measurements of C_p as a function of temperature at low temperatures and SCXRD refinement at 127 K (Fig. S2, ESI†) indicate that (5P1)$InBr_5{\cdot}2H_2O$ undergoes a structural phase transition from orthorhombic *Pnma* to monoclinic $P2_1/n$ at around 247 K (Fig. S2 and Table S1, ESI†), which is further confirmed by a low-temperature PXRD analysis (Fig. S3a, ESI†). The H-bond length also varies with the change in temperature (Fig. S1b and Table S2, ESI†). The octahedral distortion throughout the temperature range is plausibly arising from the coordination of H_2O molecule with Indium (In) center within the $[InBr_5(H_2O)]^{2-}$ octahedron (Fig. 1 and Fig. S2a and b, ESI†). The degrees of distortion of $[InBr_5(H_2O)]^{2-}$ octahedra were calculated from two elongation factors, which define the extent of variations in bond length and bond angle, respectively (eqn (S1) and (S2), ESI†).[24] The relatively high values of these factors for room-temperature and low-temperature structures of (5P1)$InBr_5{\cdot}2H_2O$ indicate a high degree of distortion in the compound (Table S3, ESI†). Fig. S4a of ESI† presents the powder X-ray diffraction (PXRD) pattern of (5P1)$InBr_5{\cdot}2H_2O$ at room temperature, which matches the simulated pattern from SCXRD analysis, suggesting phase purity. The ambient stability of (5P1)$InBr_5{\cdot}2H_2O$ was affirmed by analysing PXRD patterns of as-synthesized samples and those aged for a few days (Fig. S3b, ESI†). Thermogravimetric analysis (TGA) data, provided in Fig. S4b of ESI,† show an ∼5% drop in weight at 73 °C followed by decomposition starting at around 300 °C. The initial weight loss at 73 °C corresponds to the loss of coordinated and lattice H_2O molecules. X-Ray photoelectron spectroscopy (XPS) data at In 3d and Br 3d levels reveal the presence of +3 and −1 as the only oxidation states for In and Br, respectively (Fig. S5a and b, ESI†). Field emission scanning electron microscopy (FESEM) analysis ensures the composition and elemental homogeneity of (5P1)$InBr_5{\cdot}2H_2O$ (Fig. S6 and S7 ESI†).

Optical property investigations of (5P1)$InBr_5{\cdot}2H_2O$, carried out by taking UV-visible diffuse reflectance and PL spectroscopy measurements, show an optical bandgap of ∼3.7 eV (Fig. 2a). The PL spectrum acquired at room temperature depicts the existence of two emission peaks, centred at 423 and 637 nm (see Fig. 2b), termed as fundamental emission (FE) and self-trapped excitonic (STE) emission, respectively. The wavelengths of both the emissions are independent of excitation wavelength (λ_{ex}) although the intensities of the peaks reached a maximum at λ_{ex} of ∼365 nm. The bulk crystal emits bright pink light (inset, Fig. 2b and Fig. S8a, ESI†) under 365 nm UV radiation. The peak maximum at ∼363 nm in the photoluminescence excitation (PLE) spectrum (Fig. S8b, ESI†) matches the λ_{ex} corresponding to the maximum-intensity emission peak. (5P1)$InBr_5{\cdot}2H_2O$ demonstrates a promising photoluminescence quantum yield (PLQY) of 21.4% under 365 nm excitation at room temperature.

Temperature-dependent (75–325 K) PL experiment was conducted to explore the underlying mechanism for the broad emission of (5P1)$InBr_5{\cdot}2H_2O$. The low-temperature PL spectra reveal the presence of two emission peaks (FE and STE) at different ranges of wavelengths, with descending peak intensities upon increasing temperature as depicted in Fig. 3a. This relationship between peak intensity and temperature is attributed to the enhancement of nonradiative recombination and coupling with phonons. The STE peak undergoes a blue shift with increasing temperature up to ∼ 250 K followed by a slight red shift with further increase in temperature (Fig. S9a, ESI†). The peak shift of the STE emission with temperature can be

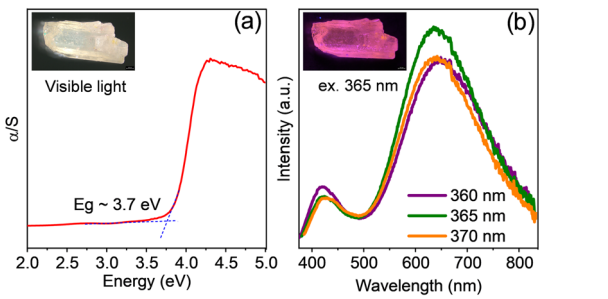

Fig. 2 (a) Electronic absorption spectrum of (5P1)$InBr_5{\cdot}2H_2O$. Inset: Optical image of a (5P1)$InBr_5{\cdot}2H_2O$ crystal under visible light. (b) Emission spectra of (5P1)$InBr_5{\cdot}2H_2O$ crystals subjected to excitations at indicated UV wavelengths. Inset picture shows pink emission from the crystal subjected to 365-nm-wavelength excitation.

elucidated with eqn (S4), ESI,† by considering the competing effects of thermal expansion (A_{TE}) and electron–phonon interactions (A_{EP}). The predominant contribution of thermal expansion results in a gradual blue shift of the PL peak position with increasing temperature up to 250 K and subsequently a lowering of peak energy with further increase in temperature due to the dominance of electron–phonon interactions. To gain better insight, temperature-dependent PL results were subjected to fitting to obtain physical parameters including the exciton binding energy (E_b), Huang–Rhys factor (S) and electron–phonon coupling coefficient. Fitting the plot in Fig. S9b (ESI†), with the following equation.[25]

$$A(T) = \frac{A(0)}{1 + \exp\left[\frac{E_b}{k_B T}\right]} \quad (1)$$

where $A(T)$ and $A(0)$ denote the integrated intensity of emission plots at temperatures T K and 0 K, respectively, and k_B is the Boltzmann constant, yields an estimated exciton binding energy (E_b) value of 120.3 ± 6.8 meV for (5P1)$InBr_5{\cdot}2H_2O$, which is significantly greater than those of reported 3D perovskite halides (*i.e.*, $MAPbX_3$ and $CsPbX_3$),[26,27] as well as room temperature thermal energy (~26 meV). The high E_b value supports the occurrence of radiative recombination in the (5P1)$InBr_5{\cdot}2H_2O$ system. The extent of electron–phonon coupling in this hybrid halide system was assessed by calculating the Huang–Rhys (S) factor from fitting the temperature-dependent full width at half maximum (FWHM) values of the STE emission with eqn (2),[25]

$$\mathrm{FWHM}\,(T) = 2.36\sqrt{S}\hbar\omega_{ph}\sqrt{\coth\left(\frac{\hbar\omega_{ph}}{2k_B T}\right)} \quad (2)$$

where ω_{ph} is the phonon frequency. Carrying out this procedure yields S and $\hbar\omega_{ph}$ values of 16.39 ± 0.61 and 29.37 ± 0.7 meV, respectively (Fig. 3b). The high S value (>10) illustrates substantial electron–phonon coupling, responsible for a broad and intense STE peak. However, the FWHM of the FE peak remains independent of temperature (Fig. S9c, ESI†).

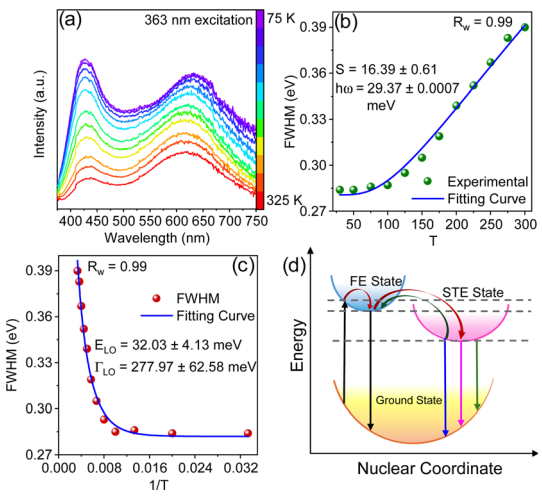

Fig. 3 (a) PL spectra of (5P1)$InBr_5{\cdot}2H_2O$ at various temperatures. (b) and (c) Plots of FWHM (in eV) *versus* (b) temperature (T) and (c) $1/T$, along with curves fitted to the data. (d) Schematic diagram for the emission mechanism in (5P1)$InBr_5{\cdot}2H_2O$. (FE = free exciton, STE = self-trapped exciton).

To gain a comprehensive understanding of individual phonon contribution to the significant electron–phonon coupling, a plot of FWHM *vs.* $1/T$ of the STE peak was fitted using the Rudin model as shown in the following equation[28]

$$\begin{aligned}\Gamma(T) &= \Gamma(0) + \Gamma_{ac} + \Gamma_{LO} \\ &= \Gamma(0) + \gamma_{ac} T + \frac{\gamma_{LO}}{\exp\left[\frac{E_{LO}}{k_B T}\right] - 1}\end{aligned} \quad (3)$$

where $\Gamma(T)$ and $\Gamma(0)$ are the FWHMs at temperatures of T K and 0 K, respectively; Γ_{ac} and Γ_{LO}, are acoustic and longitudinal optical (LO) phonon modes; γ_{ac} and γ_{LO} represent the electron-acoustic phonon coupling coefficient and electron-LO phonon coupling coefficient, respectively; and E_{LO} is the characteristic LO phonon energy. The fitting result yields γ_{LO} and E_{LO} values of 277.97 ± 62.58 meV and 32.03 ± 4.13 meV, respectively, as depicted in Fig. 3c. The high γ_{LO} value further affirms the occurrence of strong electron–phonon coupling in the lattice, which is an essential requirement for the STE emission. The analysis of optical properties shows the presence of fundamental emission originating from a higher-energy excited state, along with the emergence of a broad and intense STE emission at a higher-wavelength region from an excited state that is probably formed as a result of lattice distortion on excitation due to strong electron–phonon coupling (Fig. 3d).

STE emission is a consequence of transient lattice distortion upon photoexcitation, where the excitation-induced lattice deformation typically evolves from the soft crystal structure. (5P1)$InBr_5{\cdot}2H_2O$ possesses an exceedingly soft structure and substantial electron–phonon coupling. The low-frequency Raman modes (66, 116, 135, 173 and 222 cm^{-1}) of (5P1)$InBr_5{\cdot}2H_2O$ (Fig. 4a) are attributed to low-energy optical phonon modes (non-correlated vibrations of weakly bonded atoms), which are directly contributing to form the soft lattice. Furthermore, low temperature (2–30 K) heat capacity (C_p) measurement provides additional insight into the lattice dynamics of (5P1)$InBr_5{\cdot}2H_2O$, which indicates that the measured temperature variation of C_p (Fig. 4b) can be precisely described by incorporating three Einstein oscillator modes in the Debye–Einstein model (eqn S5, ESI†).[29] These modes have characteristic temperatures of Θ_{E1} = 23 K (~16 cm^{-1}), Θ_{E2} = 49 K (~34 cm^{-1}), and Θ_{E3} = 99 K (~68 cm^{-1}) (Table S4, ESI†). Of these Einstein modes, Θ_{E3} (~68 cm^{-1}) matches well with one of the low-frequency Raman modes (~66 cm^{-1}). The plot of C_p/T^3 *vs.* T (Fig. 4c) exhibits a boson-like peak at ~7 K, suggesting the presence of excess low-energy optical phonon density of states.

The 0D hybrid halide, due to its chemical bonding hierarchy (Fig. 1 and Fig. S2, ESI†), displays a significant amount of anharmonicity, which endows the lattice with substantial softness. A high Grüneisen parameter (γ) (measure of anharmonicity) value of 2.25, calculated from eqn (S7) of ESI† using experimental sound velocity data, attests to strong anharmonicity in the lattice. Our measurements show transverse (ν_t) and longitudinal (ν_l) sound velocities of 1035 and 2237 ms^{-1} respectively, and a mean sound velocity estimated to be 1166 ms^{-1}, which is remarkably low. The extent of softness of the crystal is characterized from bulk modulus (B) and

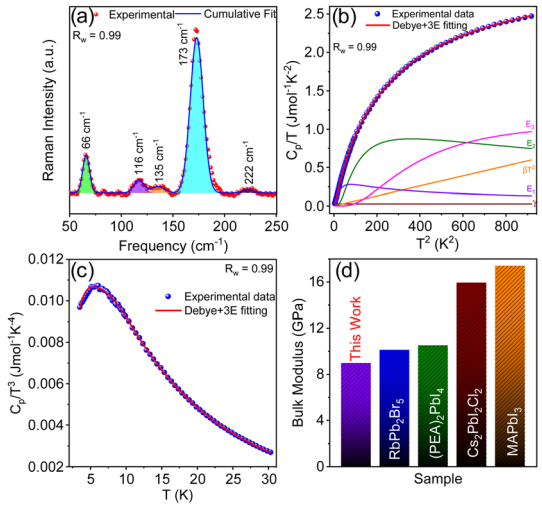

Fig. 4 (a) Room-temperature Raman spectrum of (5P1)$InBr_5{\cdot}2H_2O$. (b) Debye–Einstein fit of a plot of C_p/T *vs.* T^2 for (5P1)$InBr_5{\cdot}2H_2O$ with individual contributions from Debye (β), electronic (γ), and three Einstein modes (E_1, E_2 and E_3). (c) Plot of C_p/T^3 *vs.* T, showing a boson-like peak feature at 7 K, fitted by a combined Debye–Einstein model. (d) Comparison of bulk modulus (B) of (5P1)$InBr_5{\cdot}2H_2O$ with those of other hybrid and all-inorganic metal halides, namely $RbPb_2Br_5$,[11] $(PEA)_2PbI_4$,[30] $Cs_2PbI_2Cl_2$,[31] and $MAPbI_3$.[30]

shear modulus (G), estimated from sound velocity values (see Methods section, ESI†).[11] Our measurements show values of G and B much lower than those of all-inorganic and other hybrid halide systems (Fig. 4d and Fig. S10, ESI†).[11,30,31] The low value of the Debye temperature, Θ_D (146 K), calculated from sound velocity measurement nearly matches the Θ_D (138 K) obtained from Debye–Einstein fitting of C_p data (Fig. 4b). The low Θ_D provides concrete proof of softness in this 0D hybrid lattice of (5P1)$InBr_5{\cdot}2H_2O$, which facilitates STE emissions upon photoexcitation.

In summary, we have synthesized a new 0D hybrid halide, (5P1)$InBr_5{\cdot}2H_2O$, which displays bright pink emission due to the presence of broad STE as well as band-to-band emission peaks. The origin of the STE emission was attributed to the softness of the crystal structure, mediated by distortion-induced large anharmonicity. Low-energy optical phonon modes, tracked with Raman spectroscopy and low-temperature heat capacity measurement, confirm the presence of low-frequency vibration of weakly bonded atoms, resulting in low values of elastic moduli for the compound. Furthermore, PL measurements taken at various temperatures reveal elevated electron–phonon coupling of the soft lattice, ultimately promoting STE emission upon photoexcitation.

K. B. acknowledges support from the Swarna-Jayanti fellowship, Science and Engineering Research Board (SERB) (SB/SJF/2019-20/06), DST, India. SB acknowledges JNCASR for fellowship support. A. M. acknowledges the support from SERB National Postdoctoral Fellowship (PDF/2023/001396). KB acknowledges Abhishake Mondal, IISc for low-temperature PXRD measurement.

Data availability

The data supporting this article have been included as part of the ESI.†

Conflicts of interest

There are no conflicts to declare.

Notes and references

1 NREL. Best Research-Cell Efficiency Chart, Photovoltaic Research, NREL; 2021. Available at: https://www.nrel.gov/pv/cell-efficiency.html.
2 M. V. Kovalenko, *et al.*, *Science*, 2017, **358**, 745–750.
3 Y. Bekenstein, *et al.*, *J. Am. Chem. Soc.*, 2015, **137**, 16008–16011.
4 Q. A. Akkerman, *et al.*, *Nat. Mater.*, 2018, **17**, 394–405.
5 W. Ning and F. Gao, *Adv. Mater.*, 2019, **31**, 1900326.
6 M. Li and Z. Xia, *Chem. Soc. Rev.*, 2021, **50**, 2626–2662.
7 P. Acharyya, *et al.*, *Nat. Commun.*, 2022, **13**, 5053.
8 L. Zhou, *et al.*, *Adv. Opt. Mater.*, 2021, **9**, 2100544.
9 J. E. Thomaz, *et al.*, *J. Am. Chem. Soc.*, 2020, **142**, 16622–16631.
10 B. M. Benin, *et al.*, *Angew. Chem., Int. Ed.*, 2018, **57**, 11329–11333.
11 J. Pradhan, *et al.*, *Chem. Sci.*, 2022, **13**, 9952–9959.
12 V. Morad, *et al.*, *J. Am. Chem. Soc.*, 2019, **141**, 9764–9768.
13 I. Maria, *et al.*, *J. Am. Chem. Soc.*, 2023, **145**, 9292–9303.
14 R. Zhang, *et al.*, *Angew. Chem., Int. Ed.*, 2019, **58**, 2725–2729.
15 L.-J. Xu, *et al.*, *Nat. Commun.*, 2020, **11**, 4329.
16 X. Jiang, *et al.*, *ChemSusChem*, 2019, **12**, 5228–5232.
17 X. Yuan, *et al.*, *Nanoscale*, 2012, **4**, 1968–1971.
18 J. Dědeček and B. Wichterlová, *Phys. Chem. Chem. Phys.*, 1999, **1**, 629–637.
19 L. Zhou, *et al.*, *Angew. Chem., Int. Ed.*, 2019, **58**, 5277–5281.
20 L. Zhou, *et al.*, *Angew. Chem., Int. Ed.*, 2019, **58**, 15435–15440.
21 D. Chen, *et al.*, *Inorg. Chem.*, 2019, **58**, 15602–15609.
22 A. S. Kshirsagar, *et al.*, *J. Phys. Chem. C*, 2021, **125**, 27671–27677.
23 Y. Jing, *et al.*, *Chem. Mater.*, 2020, **32**, 5327–5334.
24 A. Mandal, *et al.*, *Chem. Sci.*, 2023, **14**, 9770–9779.
25 A. Mandal, *et al.*, *J. Phys. Chem. Lett.*, 2022, **13**, 9103–9113.
26 H. Yang, *et al.*, *Chem. Mater.*, 2017, **29**, 8978–8982.
27 M. Baranowski and P. Plochocka, *Adv. Energy Mater.*, 2020, **10**, 1903659.
28 S. Rudin, *et al.*, *Phys. Rev. B: Condens. Matter Mater. Phys.*, 1990, **42**, 11218–11231.
29 J. Pradhan, *et al.*, *Chem. Mater.*, 2024, **36**, 3405–3416.
30 S. Rathore, *et al.*, *J. Alloys Compd.*, 2023, **936**, 168328.
31 P. Acharyya, *et al.*, *J. Am. Chem. Soc.*, 2020, **142**, 15595–15603.

